

High-Order Adaptive Extended Stencil FEM (AES-FEM) with Linear Elements

Rebecca Conley

Tristan J. Delaney

Xiangmin Jiao

June 15, 2019

Abstract

The finite element methods and their high-order variants are powerful tools for solving partial differential equations on complex, but they are highly dependent on good element quality. In this paper, we present a high-order extension of the adaptive extended stencil FEM (AES-FEM), which is independent of element quality. AES-FEM replaces the traditional interpolatory basis functions of FEM with *generalized Lagrange polynomial basis functions*, which are calculated via a local weighted least-squares approximation. The method preserves the theoretical framework of FEM, and allows imposing essential boundary conditions and integrating the stiffness matrix in the same way as the classical FEM. We describe the formulation of AES-FEM and its extension to high-order using meshes with only linear elements. We present numerical results in 2D and 3D for the Poisson equation and the time-independent convection-diffusion equation, including results on curved boundaries. As the results demonstrate, AES-FEM is more accurate than FEM, is more stable on meshes with poor quality elements, has better efficiency in terms of runtime versus error, and is easier to use for complex geometries with curved boundaries.

Key Words: finite element methods; partial differential equations; curved boundaries; high-order accuracy; stability; weighted least squares

1 Introduction

Finite element methods (FEM) are one of the most important tools for solving partial differential equations on complex geometries. FEM originated as a second order accurate method, but for several decades, researchers have been exploring high-order variants. In this paper, we use the term “high-order” to refer to any method of third or greater order accuracy. Some high-order methods include isoparametric FEM [12], hp -FEM [10], discontinuous Galerkin method [8], spectral element method [5], and isogeometric analysis [17]. Despite the fact that these methods can reach exponential convergence under appropriate conditions, high-order methods have remained largely confined to academic study and has yet to make much of an impact in industry [33]. This is due to many

reasons, not least of which is that high-order schemes are generally less robust [35] and generating good quality meshes for high-order methods is still not fully resolved [24].

The finite element methods have a strong dependence on element quality and a few “bad” elements can result in an ill-conditioned linear system. This can lead to slowly converging iterative solvers and even a loss of accuracy. This problem is even more acute for high-order methods. It is well known that a high-order mesh must conform to the curved boundaries of the physical domain otherwise the geometric error will dominate and the method will not be able to achieve high-order convergence [4]. The Jacobian determinate of the mapping from the reference element to the physical element must be positive everywhere in the reference element for the element to be geometrically valid. This is particularly difficult to achieve in 3D [14].

In this paper, we present a high order version of the adaptive extended stencil finite element method or AES-FEM (pronounced “ace”-F-E-M), which addresses the problem of element quality dependence for high-order methods. AES-FEM is independent of element quality. Furthermore, AES-FEM uses linear meshes and thus avoids the issues introduced by using elements with curved boundaries. AES-FEM replaces the piecewise polynomial Lagrange basis functions of the traditional FEM with an alternative set of basis functions. These basis functions are computed using weight least squares over an adaptively extendable stencil. We call these basis functions *generalized Lagrange polynomial basis functions (GLPBF)*. AES-FEM fits within the theoretical framework of FEM. Imposition of essential boundary conditions and numerical quadrature are performed the same way as traditional FEM.

The remainder of the paper is organized as follows. Section 2 discusses the background and discuss some related methods. Section 3 presents the formulation of AES-FEM. Section 4 extends AES-FEM to high-order accuracy. Section 5 contains the results of numerical experiments including accuracy, stability, and efficiency. Section 6 concludes with a discussion and future work.

2 Background and Related Work

In this section, we present the weighted residual formulation of the finite element method and we discuss several high-order finite element methods related to AES-FEM.

2.1 Weighted Residual Formulation of FEM

AES-FEM starts from the weighted residual formulation. Details about the weighted residual methods can be found in [13]. Here we include a derivation for completeness.

Consider a linear differential operator \mathcal{L} defined on a bounded, simply-connected domain Ω , with outward unit normal vector \mathbf{n} . Denote the boundary of Ω as $\Gamma = \Gamma_D \cup \Gamma_N$, where Γ_D and Γ_N are disjoint sets on which Dirichlet

and Neumann boundary conditions are specified, respectively. We want to find a function u such that

$$\mathcal{L}u = f \quad (1)$$

subject to the boundary conditions

$$u = g \text{ on } \Gamma_D \quad \text{and} \quad \frac{\partial u}{\partial \mathbf{n}} = h \text{ on } \Gamma_N. \quad (2)$$

Eq. (1) is the strong form of the PDE. In the weighted residual formulation, we use the weak form based on a set of weight functions $\Psi = \{\psi_1, \dots, \psi_n\}$, by requiring the residual $\mathcal{L}u - f$ to be orthogonal to ψ_i , i.e.,

$$\int_{\Omega} \psi_i (\mathcal{L}u - f) \, dV = 0. \quad (3)$$

To approximate u , let $\Phi = \{\phi_1, \dots, \phi_n\}$ be a set of basis functions define an approximation

$$u \approx \sum_{j=1}^n u_j \phi_j. \quad (4)$$

Substituting (4) into the weak form (3) and rearranging the equations, we then obtain

$$\sum_{j=1}^n u_j \int_{\Omega} \psi_i (\mathcal{L}\phi_j) \, dV = \int_{\Omega} \psi_i f \, dV. \quad (5)$$

At this point for simplicity, let us consider the Poisson equation with Dirichlet boundary conditions, for which the weak form is given by

$$\int_{\Omega} \psi_i \nabla^2 u \, dV = \int_{\Omega} \psi_i f \, dV. \quad (6)$$

Substituting (4) into (6), we obtain

$$\sum_{j=1}^n u_j \int_{\Omega} \psi_i \nabla^2 \phi_j \, dV = \int_{\Omega} \psi_i f \, dV. \quad (7)$$

The finite element method uses integration by parts to reduce the order of derivatives required by (7). If ψ_i has weak derivatives and satisfies the condition $\psi_i|_{\Gamma_D} = 0$, then after integrating by parts and imposing the boundary conditions, we arrive at

$$-\sum_{j=1}^n u_j \int_{\Omega} \nabla \psi_i \cdot \nabla \phi_j \, dV = \int_{\Omega} \psi_i f \, dV. \quad (8)$$

Taking (8) over the n weight functions, we obtain the linear system

$$\mathbf{K}\mathbf{u} = \mathbf{g}, \quad (9)$$

where \mathbf{K} is the stiffness matrix and \mathbf{g} is the load vector, with

$$k_{ij} = - \int_{\Omega} \nabla \psi_i \cdot \nabla \phi_j \, dV \quad \text{and} \quad g_i = \int_{\Omega} \psi_i f \, dV. \quad (10)$$

If the weight functions are chosen to be the same as the basis functions then we will arrive at the Galerkin method. In AES-FEM, generalized Lagrange polynomial basis functions are chosen for the basis functions and the weight functions are taken to be the standard (“hat”) FEM test functions.

2.2 High-Order Finite Element Methods

The isoparametric finite element method uses the same (often, high-order polynomial) shape functions to define both the geometry and the functional approximation [37, 12]. If the boundary of the domain is curved, a high-order approximation of the geometry is necessary for the accuracy of the solution to be high-order [4]. The use of isoparametric elements demands a high quality mesh. If an element is too distorted then a one-to-one mapping between reference element and the physical element no longer exists, and the method will break down [37]. While progress has been made to address the meshing requirements, there are still open questions, especially for high-order elements in 3D [19, 32].

The p -version of the finite element method increases the degree of the basis functions towards infinity while holding the refinement of the mesh constant [30, 2]. This can be combined with the h -version of FEM, in which the elements are refined, to form hp -FEM [29]. The hp -FEM can achieve exponential convergence provided that the mesh is optimal [10]. One major challenge of hp -FEM is guaranteeing the inter-element continuity of the shape functions. This can be addressed by using constraints [28], although this is algorithmic complex, especially in 3D. Another strategy is multi-level hp -adaptivity, which uses a coarse mesh everywhere and then overlays finer meshes in areas of interest [36]. The continuity of the shape functions is guaranteed by construction.

AES-FEM requires meshes with linear elements and is independent of mesh quality. Accurate representation of complex geometry is relatively simple for linear elements as compared to isoparametric elements, and hence AES-FEM avoids these open problems concerning meshes.

2.3 Discontinuous Galerkin and Spectral Element Methods

Spectral methods use infinitely differentiable, global basis functions in the weighted residual formulation for solving differential equations [5]. They are able to achieve exponential convergence provided the solution is smooth. However, they are not applicable to complex geometries [20]. The spectral element method, which divides the domain into quadrilaterals, was introduced to better handle more general geometries [22]. Quadrilaterals may still be too restrictive to

model complex geometries, and hence triangle- and tetrahedron-based spectral element methods have been used [31]. Standard Gaussian quadrature cannot be used with triangle spectral element method, and it is still somewhat of an open question as to where to place the nodes on triangles and tetrahedra [21]. AES-FEM utilizes standard Gaussian quadrature rules to perform the numerical integration.

Similar to FEM, discontinuous Galerkin (DG) methods start with a weak form of the governing equation. Continuity of the basis and test functions between elements is not enforced, instead a numerical flux is used at the element boundaries. During the 1970s, interior penalty methods for elliptical problems were developed, and these methods and DG can be unified under one framework [1]. DG methods are able to achieve high accuracy and can be used on complex geometries [8]. High-order accurate DG methods have been applied to the Navier-Stokes and compressible Euler equations [4, 3]. More recent developments include compact DG [23], which has a more compact stencil than local DG methods, and hybridized DG [7], which has a relatively low number of degrees of freedom. Unlike DG, AES-FEM uses basis functions that have inter-element continuity.

2.4 Isogeometric Analysis and Other Methods with Splines

Isogeometric analysis (IGA) uses NURBS (Non-Uniform Rational B-Splines) or T-splines as basis functions instead of the standard FEM basis functions [17]. These methods can deliver high accuracy over very coarse meshes and can be advantageous for problems that can benefit from high-degree continuity, such as thin-shell modeling. However, IGA does not alleviate the dependency on mesh quality, since NURBS in effect impose stronger requirement on mesh quality than the standard FEM.

Another recent development is NURB-enhanced finite element method (NE-FEM) which uses NURBS to represent the boundary of the computational domain and standard piecewise polynomials for approximating the solution [25].

3 Formulation of AES-FEM

3.1 Weighted Least Squares Approximations

In this subsection, we describe numerical differentiation based on weighted least-squares approximations as described in [18, 34] and then explain how to compute the generalized Lagrange polynomial basis functions, following the method in [9].

We begin by considering the Taylor series expansion of a bivariate function $f(\mathbf{u})$ with at least $d + 1$ continuous derivatives in some neighborhood of $\mathbf{u}_0 = (0, 0)$. Denote $c_{jk} = \frac{\partial^{j+k}}{\partial u^j \partial v^k} f(\mathbf{u}_0)$. Then for any \mathbf{u} in the neighborhood, f may

be approximated to the $(d + 1)$ st order accuracy about the origin \mathbf{u}_0 as

$$f(\mathbf{u}) = \underbrace{\sum_{p=0}^d \sum_{j,k \geq 0}^{j+k=p} c_{jk} \frac{u^j v^k}{j! k!}}_{\text{Taylor Polynomial}} + \underbrace{\mathcal{O}(\|\mathbf{u}\|^{d+1})}_{\text{remainder}}. \quad (11)$$

Note that analogous formulae exist in 1D and 3D. The coefficients c_{jk} are unknown and we compute them as follows.

We select a stencil of m nodes from the neighborhood around \mathbf{u}_0 , and locally parameterize the neighborhood such that \mathbf{u}_0 is located at the origin $(0, 0)$. Substituting the locally parametrized neighboring points into (11), we obtain a set of approximate equations

$$\sum_{p=0}^d \sum_{j,k \geq 0}^{j+k=p} c_{jk} \frac{u_i^j v_i^k}{j! k!} \approx f_i, \quad (12)$$

where $f_i = f(\mathbf{u}_i)$ and the c_{jk} denote the unknowns. There are $n = (d + 1)(d + 2)/2$ unknowns in 2D and $n = (d + 1)(d + 2)(d + 3)/6$ unknowns in 3D. Let \mathbf{V} denote the generalized Vandermonde matrix, \mathbf{c} denote the vector of unknowns (i.e., the c_{jk}) and \mathbf{f} denote the vector of function values. Then we arrive at the rectangular system of size $m \times n$

$$\mathbf{V}\mathbf{c} \approx \mathbf{f}. \quad (13)$$

We use a weighted linear least-squares formulation [16] to solve (13). We minimize a weighted norm (or semi-norm)

$$\min_{\mathbf{c}} \|\mathbf{V}\mathbf{c} - \mathbf{f}\|_{\mathbf{W}} \equiv \min_{\mathbf{c}} \|\mathbf{W}(\mathbf{V}\mathbf{c} - \mathbf{f})\|_2, \quad (14)$$

where \mathbf{W} is an $m \times m$ diagonal weighting matrix. Denoting the diagonal entries of \mathbf{W} as w_i , the i th row of matrix \mathbf{V} is assigned the weight w_i . We assign heavier weights to nodes that are closer to \mathbf{u}_0 , thus prioritizing them. We could also filter out undesirable points by setting their weight very close to or equal to zero. Note that for a given node, the weighting matrix \mathbf{W} is constant. Note that if \mathbf{f} is not in the column space of \mathbf{V} then different choices of the weighting scheme can lead to different solutions. If \mathbf{f} is in the column space, then a nonsingular weighting matrix does not affect the solution.

We compute the weights as follows. Let h denote the maximum radius of the neighborhood, that is

$$h = \max_{1 \leq i \leq m} \{\|\mathbf{u}_i\|_2\}. \quad (15)$$

Then

$$w_i = \left(\frac{\|\mathbf{u}_i\|_2}{h} + \epsilon \right)^{-1}, \quad (16)$$

where some small number ϵ , such as $\epsilon = 0.01$, is added to avoid division by zero. After the weighting matrix has been applied, we arrive at a new system

$$\mathbf{M}\mathbf{c} \approx \tilde{\mathbf{f}}, \quad \text{where } \mathbf{M} = \mathbf{WV} \text{ and } \tilde{\mathbf{f}} = \mathbf{Wf}. \quad (17)$$

We employ a diagonal scaling matrix \mathbf{S} to address the issue of poor scaling of the columns of \mathbf{WV} . Poor scaling can lead to ill-conditioning of the the linear system, which in turn can lead to loss of accuracy due to rounding errors. Let \mathbf{a}_j denote the j th column of an arbitrary matrix \mathbf{A} . A typical choice for the j th entry of \mathbf{S} is either $1/\|\mathbf{a}_j\|_2$, which approximately minimizes the 2-norm condition number of \mathbf{AS} [16], or $1/\|\mathbf{a}_j\|_\infty$ [6]. Using exact arithmetic, the matrix \mathbf{S} does not affect the solution. After applying the scaling matrix to \mathbf{WV} , the problem becomes

$$\min_{\mathbf{d}} \|\tilde{\mathbf{V}}\mathbf{d} - \tilde{\mathbf{f}}\|_2, \quad \text{where } \tilde{\mathbf{V}} \equiv \mathbf{WV}\mathbf{S} = \mathbf{MS} \text{ and } \mathbf{d} \equiv \mathbf{S}^{-1}\mathbf{c}. \quad (18)$$

Conceptually, the solution to the above problem may be reached through the use of a pseudoinverse. We will have

$$\mathbf{d} = \tilde{\mathbf{V}}^+ \tilde{\mathbf{f}} \quad \text{where } \tilde{\mathbf{V}}^+ \equiv (\tilde{\mathbf{V}}^T \tilde{\mathbf{V}})^{-1} \tilde{\mathbf{V}}^T. \quad (19)$$

Since the resulting system may still be rank-deficient or ill-conditioned, in practice, we solve it using QR factorization with column pivoting. Finally, we have computed the vector of partial derivatives for the Taylor polynomial

$$\mathbf{c} = \mathbf{S}\mathbf{d}. \quad (20)$$

3.2 Generalized Lagrange Polynomial Basis Functions

Let us now introduce some notation to allow us to write the Taylor series and the set of generalized Lagrange polynomial basis functions in matrix notation. Let $\mathcal{P}_k^{(d)}(\mathbf{x})$ denote the set of all k -dimensional monomials of degree d and lower, stored in ascending order as a column vector. If there are no ambiguities, we will simply use \mathcal{P} . Let \mathbf{D} be a diagonal matrix consisting of the fractional factorial part of the coefficients, i.e. $\frac{1}{j!k!}$ in (11). Then we may write the truncated Taylor series as

$$f(\mathbf{x}) = \mathbf{c}^T \mathbf{D} \mathcal{P}(\mathbf{x}). \quad (21)$$

Given a stencil of nodes about a point \mathbf{u}_0 , we use weighted least-squares approximations as described in the previous section to compute the associated set Φ of generalized Lagrange polynomial basis functions. When computing the j th basis function ϕ_j , let $\mathbf{f} = \mathbf{e}_j$, where \mathbf{e}_j is the j th column of the identity matrix. Following (19) and (20), we have

$$\mathbf{c} = \mathbf{S} \tilde{\mathbf{V}}^+ \mathbf{W} \mathbf{e}_j. \quad (22)$$

Thus for the j th basis function, the vector \mathbf{c} is exactly the j th column of $\mathbf{S}\tilde{\mathbf{V}}^+\mathbf{W}$. We define a set of basis functions as

$$\Phi = \left(\mathbf{S}\tilde{\mathbf{V}}^+\mathbf{W} \right)^T \mathbf{D}\mathbf{P}. \quad (23)$$

Note that since \mathbf{W} and \mathbf{S} are constant for a given stencil, Φ is a set of polynomials. The following properties hold for the basis functions in (23), as shown in Theorem 2 of [9]. For any set of degree- d generalized Lagrange polynomial basis functions $\{\phi_i\}$:

1. $\sum_i f(x_i) \phi_i$ approximates a function f to $\mathcal{O}(h^{d+1})$ in a neighborhood of the stencil, where h is some characteristic length measure, and
2. $\sum_i \phi_i = 1$.

We refer to these properties as *function value as coefficient* and *partition of unity*, respectively. These properties ensure the consistency and also allow the Dirichlet boundary conditions to be easily imposed.

4 High-Order AES-FEM

In this section we present high-order AES-FEM, including a description of high-order AES-FEM, analysis, and implementation details.

4.1 Description

The AES-FEM starts from the weighted residual formulation for FEM, as given in (8). The basis functions of AES-FEM are GLP basis functions and the weight functions are traditional FEM “hat” functions. For a given node i and its associated weight function ψ_i , a set of GLP basis functions Φ is constructed on a stencil of neighboring points. This weight function ψ_i and its associated GLP basis functions Φ are used to construct the i th row of the stiffness matrix, as given in (10). Note that because a different set of GLP basis functions is associated with each weight function, the basis functions on a given element differ row to row in the stiffness matrix.

4.2 Implementation Details

One very important implementation detail is neighborhood selection. We use an Array-based Half Facet (AHF) data structure to store the mesh [11], which allows efficient neighborhood selection. Details are discussed in this subsection.

4.2.1 Mesh Data Structure

In a d -dimensional mesh, the term *facet* refers to the $(d-1)$ -dimensional mesh entities; that is, in 2D the facets are the edges, and in 3D the facets are the faces. The Array-based Half-Facet data structure is based on the concept the

every facet in a manifold mesh consists of two half-facets that are oriented in opposite directions. These two half-facets are *sibling half-facets*. Half-facets on the boundary of the domain have no siblings. Each half-facet is identified by a two tuple: the element ID and a local facet ID within the element. In 2D, we store the element connectivity, sibling half-edges, and a mapping from each node to an incident half-edge. In 3D, we store the element connectivity, sibling half-faces, and a mapping from each node to an incident half-face.

4.2.2 Neighborhood Selection

The *1-ring neighbor elements* of a node are defined to be the elements incident on the node. The *1-ring neighborhood* of a node contains the nodes of its 1-ring neighbor elements [18]. Often the 1-ring neighborhood of a node supplies the appropriate number of nodes for constructing quadratic GLP basis functions. For high-order basis functions, it is necessary to expand the stencil and collect more nodes. Therefore, for any integer $k \geq 1$, we define the *$(k+1)$ -ring neighborhood* as the nodes in the k -ring neighborhood plus their 1-ring neighborhoods.

As k increases, the average size of the k -ring neighborhood grows very quickly. The granularity can be fine-tuned by using fractional rings. In 2D we use half-rings, which are defined in [18]; for any integer $k \geq 1$ the *$(k+1/2)$ -ring neighborhood* is the k -ring neighborhood plus the nodes of all the faces that share an edge with the k -ring neighborhood. See Figure 1 for a visualization of rings and half-rings in 2D. For 3D, we use $1/3$ - and $2/3$ -rings, as defined in [9]. For any integer $k \geq 1$, the *$(k+1/3)$ -ring neighborhood* contains the k -ring neighborhood plus the nodes of all elements that share a face with the k -ring neighborhood. The *$(k+2/3)$ -ring neighborhood* contains the k -ring neighborhood plus the nodes of all faces that share an edge with the k -ring neighborhood.

For 2D triangular meshes, typically the 1-ring has a sufficient number of nodes for quadratic basis functions. The $1^{1/2}$ -ring, 2-ring, $2^{1/2}$ -ring, and 3-ring typically provide a sufficient number of nodes for degree 3 to 6 basis functions, respectively. For 3D tetrahedral meshes, the 1-ring, $1^{1/3}$ -ring, $1^{2/3}$ -ring, 2-ring, and $2^{1/3}$ -ring have a sufficient number of nodes for degrees 2 to 6 basis functions, respectively. If the neighborhood does not provide enough points, the stencil is extended to a larger ring. This allows AES-FEM to overcome element-quality dependence and also improves its local stability.

4.3 Accuracy

The order of convergence depends on the degree of the basis functions used. We recall Theorem 1 from [9].

Theorem 1. *Suppose u is smooth and thus $\|\nabla u\|$ is bounded. Then, when solving the Poisson equation using AES-FEM with degree- d GLP basis functions in (8), for each ψ_i the weak form (6) is approximated to $\mathcal{O}(h^d)$, where h is some characteristic length measure of the mesh.*

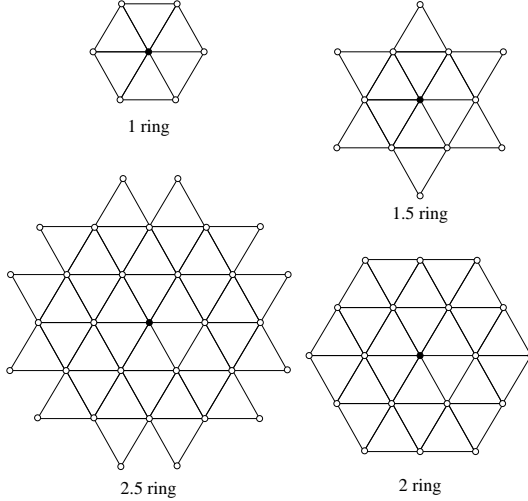


Figure 1: Examples of 2D stencils with 1-ring, 1.5-ring, 2-ring, and 2.5-ring neighborhoods of center node (in solid black).

Thus the truncation error of the weak form is of the order of the approximation of the GLP basis functions. As long as the method is stable, the rounding errors do not dominate the truncation errors, and there is no systematic cancellation of truncation errors, we expect the solution to converge at the same rate as the local truncation errors. For even-degree basis functions, this holds true, as we will see in Section 5. However, for odd-degree basis functions, the situation is more complicated due to cancellation of truncation errors, which we will analyze hereafter.

4.3.1 Cancelation of terms

When using AES-FEM with odd degree basis functions, the convergence is one degree lower than expected. This is due to canceling of leading coefficients when integrating. We prove this rigorously for the 1-D case.

Consider the weight function ψ associated with the node $x = 0$. The support of ψ is the elements $[-l_1, 0]$ and $[0, l_2]$. The weight function ψ is a hat function and thus is symmetric about zero, i.e. $\psi(x) = \psi(-x)$ and $\psi'(x) = -\psi'(-x)$. Consider the function $f(x) = \frac{1}{m+1}x^{m+1}$ where m is an even integer. Then on the element $[-l_1, 0]$

$$\int_{-l_1}^0 \psi'(x) \cdot f'(x) \, dx = \int_{-l_1}^0 \psi'(x) \cdot x^m \, dx$$

Do a change of variables $y = -x$ and recall that m is even:

$$\int_{l_1}^0 \psi'(-y) \cdot (-y)^m (-dy) = \int_{l_1}^0 -\psi'(-y) \cdot y^m \, dy = \int_{l_1}^0 \psi'(y) \cdot y^m \, dy$$

To summarize, we have

$$\int_{-l_1}^0 \psi'(x) \cdot f'(x) dx = \int_{l_1}^0 \psi'(x) \cdot f'(x) dx$$

Integrating the weak form over both elements, we have

$$\begin{aligned} \int_{\Omega} \psi' \cdot f' &= \int_{-l_1}^0 \psi' \cdot f' dx + \int_0^{l_2} \psi' \cdot f' dx \\ &= \int_{l_1}^0 \psi' \cdot f' dx + \int_0^{l_2} \psi' \cdot f' dx \\ &= \int_{l_1}^{l_2} \psi' \cdot f' dx \end{aligned}$$

Therefore if $l_1 \approx l_2$ the integral will be close to zero.

4.3.2 Curved Geometry

It is well known that if the geometry of the domain is not represented to a high enough degree, the errors from the geometric discretization will dominate and the method will not achieve high-order convergence. AES-FEM builds the high-order basis functions on stencils of nodes contained in linear meshes as discussed in the previous section. Linear meshes use h -refinement to model the geometry to the appropriate level of accuracy. Because the elements are not curved, it is simpler and more robust to achieve the desired accuracy.

5 Numerical Results

In this section, we compare the accuracy, efficiency, and element shape quality dependence of AES-FEM with degree two, four, and six basis functions and FEM with linear, quadratic and cubic basis functions. The errors are calculated using the discrete L_2 and L_{∞} norms. Let u denote the exact solution and let \hat{u} denote the numerical solution. Then, we calculate the norms as

$$L_2(\text{error}) = \left(\int_{\Omega} |\hat{u} - u|^2 \partial \Omega \right)^{1/2} \quad \text{and} \quad L_{\infty}(\text{error}) = \max_i |\hat{u} - u|. \quad (24)$$

On a series of meshes of different grid resolution, we calculate the average convergence rate as

$$\text{convergence rate} = -\log_2 \left(\frac{\text{error on } m_c}{\text{error on } m_f} \right) \Big/ \log_2 \left(\sqrt[d]{\frac{\text{nodes in } m_c}{\text{nodes in } m_f}} \right), \quad (25)$$

where d is the spacial dimension, m_c is the coarsest mesh, and m_f is the finest mesh.

5.1 2-D Results

In this section, we describe the results from our experiments in 2D. The linear meshes were created using Triangle [26] and the high-order meshes were created using Gmsh [15]. We consider two domains: the unit square and the unit circle. The meshes for the unit square range in size from 1,027 to 146,077 degrees of freedom. The meshes for the unit circle range in size from 544 to 79,417 degrees of freedom. These meshes all have good element-quality. For any element in any of the meshes, the minimum angle is 24.04 degrees, the maximum angle is 128.17 degrees and the maximum aspect ratio is 2.44, where the aspect ratio of an element is defined to be the ratio of the element's longest edge to its shortest edge.

5.1.1 Poisson Equation

We first present results for the Poisson equation with Dirichlet boundary conditions on the unit square and on the unit circle. That is,

$$-\nabla^2 u = f \quad \text{in } \Omega, \quad (26)$$

$$u = g \quad \text{on } \partial\Omega. \quad (27)$$

For the unit square, $\Omega = [0, 1]^2$, we consider the following three analytic solutions:

$$u_1 = 16x^3(1 - x^3)y^3(1 - y^3), \quad (28)$$

$$u_2 = \cos(\pi x) \cos(\pi y), \quad (29)$$

$$u_3 = \frac{1}{\sinh \pi \cosh \pi} \sinh(\pi x) \cosh(\pi y). \quad (30)$$

For the unit circle $\Omega = \{(x, y) | x^2 + y^2 \leq 1\}$, we consider the analytic solution u_3 and also

$$u_4 = \cos\left(\frac{\pi}{2}(x^2 + y^2)\right).$$

The Dirichlet boundary conditions are obtained from the given analytic solutions. On the unit square, the boundary conditions for u_1 are homogeneous and they are non-homogenous for u_2 and u_3 . On the unit circle, the boundary conditions are non-homogenous for u_3 and they are homogeneous for u_4 .

The L_∞ and L_2 norm errors for u_1 on the unit square are displayed in Figure 2. The L_2 norm errors for u_2 and u_3 on the unit square and for u_3 and u_4 on the unit circle are in Figures 3 and 4 respectively. Quadratic AES-FEM and linear FEM are very similar in terms of errors on both domains. Quartic and degree 6 AES-FEM are more accurate than quadratic and cubic FEM on the unit square. Quartic AES-FEM and cubic FEM have similar errors on the unit circle.

For solving the linear system resulting from AES-FEM, we use GMRES with ILU as a preconditioner. For FEM, we use conjugate gradient, with incomplete Cholesky as the preconditioner. The tolerance for the solvers is 10^{-12} . The drop tolerance for the preconditioners is 10^{-4} for problems on the unit square

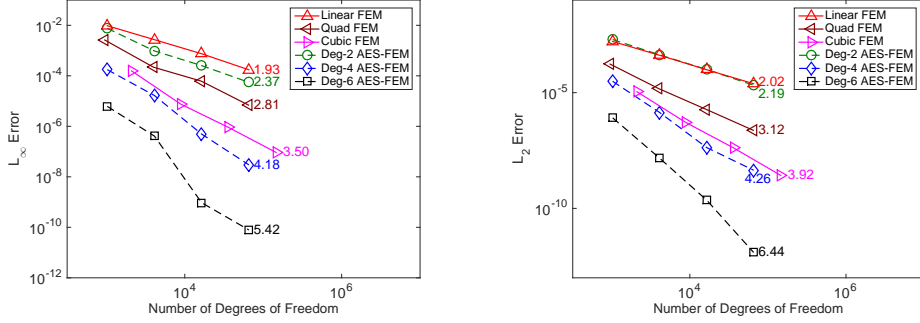


Figure 2: The errors for 2D Poisson equation on the unit square for u_1 in the infinity norm (left) and L_2 norm (right).

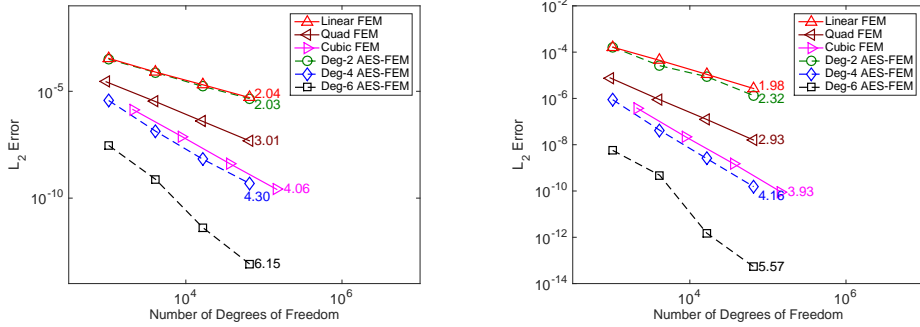


Figure 3: The L_2 norm errors for 2D Poisson equation on the unit square for u_2 (left) and u_3 (right).

and 10^{-6} for the problems on the unit circle. For the finest mesh on the unit square, the solver stagnated for cubic FEM. For the finest meshes on the unit circle, the solver stagnated for linear, quadratic and cubic FEM.

5.1.2 Convection-Diffusion Equation

We consider the time-independent convection-diffusion equation with Dirichlet boundary conditions on the unit square and on the unit circle, that is,

$$-\nabla^2 u + \mathbf{c} \cdot \nabla u = f \quad \text{in } \Omega, \quad (31)$$

$$u = g \quad \text{on } \partial\Omega. \quad (32)$$

We take $\mathbf{c} = [1, 1]^T$ for all of our tests and we consider the same analytic solutions as for the Poisson equation. Again the boundary conditions are obtained from the given analytic solutions.

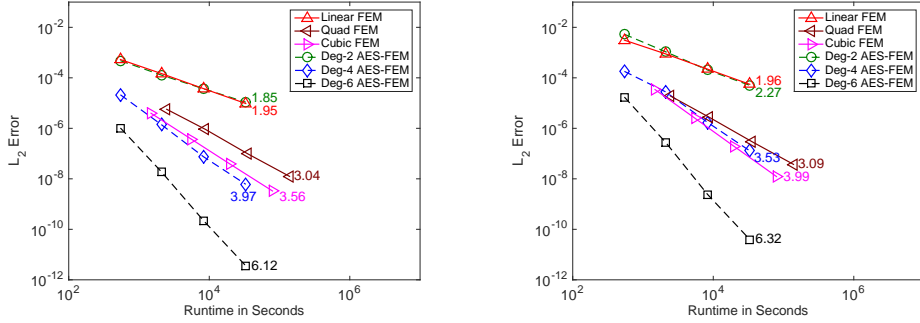


Figure 4: The L_2 norm errors for 2D Poisson equation on the unit circle for u_3 (left) and u_4 (right).

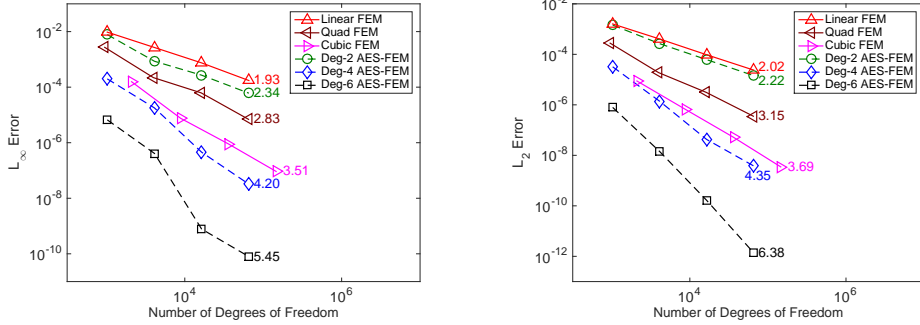


Figure 5: The errors for 2D convection-diffusion equation on the unit square for u_1 in the infinity norm (left) and the L_2 norm (right).

The L_∞ and L_2 norm errors for u_1 on the unit square are displayed in Figure 5. The L_2 norm errors for u_2 and u_3 on the unit square and for u_3 and u_4 on the unit circle are in Figures 6 and 7 respectively. Quadratic AES-FEM and linear FEM are similar in terms on convergence rate, with quadratic AES-FEM having slightly lower errors. Quartic and degree 6 AES-FEM are more accurate the quadratic and cubic FEM on the unit square and on the unit circle for u_3 . On the unit circle for u_4 , quartic AES-FEM and cubic FEM have similar errors, with cubic FEM converging at a faster rate.

For solving the linear system resulting from AES-FEM, we use GMRES with a tolerance of 10^{-12} and ILU as a preconditioner with a drop tolerance of 10^{-4} .

5.1.3 Assessment of Element-Quality Dependence

We assess the dependence of AES-FEM and FEM on element quality by solving the Poisson equation on the unit square with each method on a series of meshes

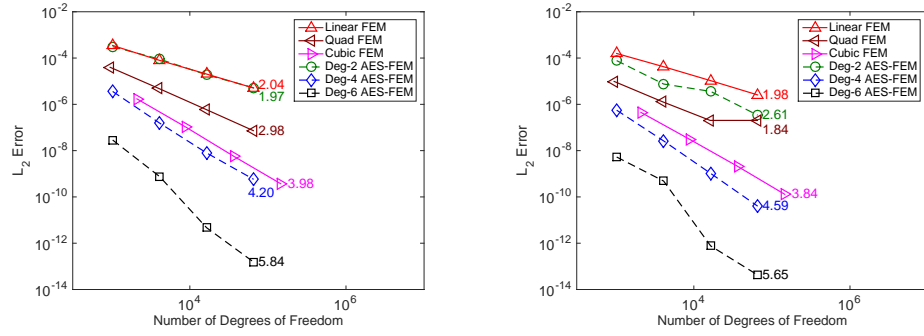


Figure 6: The L_2 norm errors for 2D convection-diffusion equation on the unit square for u_2 (left) and u_3 (right).

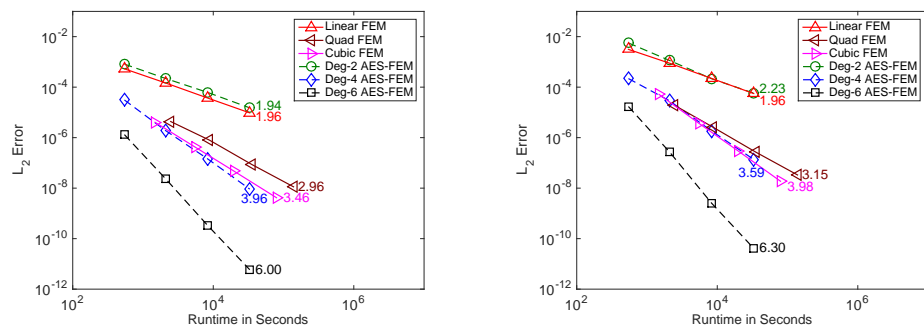


Figure 7: The L_2 norm errors for 2D convection-diffusion equation on the unit circle for u_3 (left) and u_4 (right).

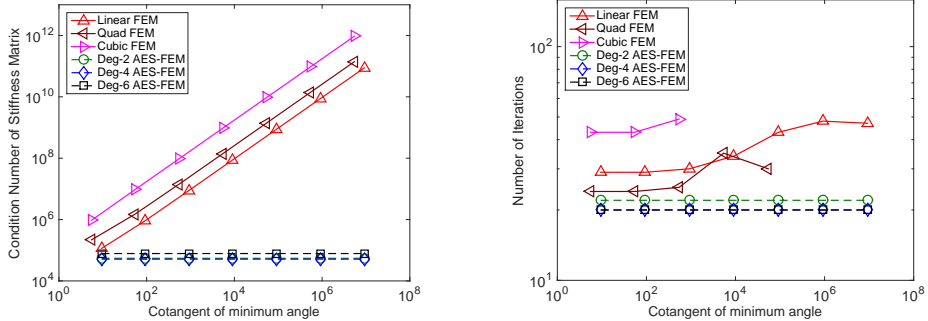


Figure 8: The lower bound of the condition numbers (left) of the stiffness matrices of FEM and AES-FEM method on a series of progressive worse meshes in 2D. The number of iterations (right) required for the iterative solver to converge when solving the corresponding systems.

with progressively worse element quality. We consider the condition numbers of the resulting stiffness matrices, the number of iterations needed to solve the resulting system, and the errors of the solutions. For all the methods, 0.003 percent of the total number of elements in the mesh are selected to be distorted. Within the selected elements, one vertex is moved incrementally towards its opposite edge. For linear FEM and AES-FEM with quadratic, quartic and degree six basis functions, we use a mesh with 130,288 elements and 65,655 degrees of freedom. Four elements are selected for distortion. For quadratic FEM, we use a mesh with 32,292 elements and 261,597 degrees of freedom. Four elements are selected. For cubic FEM, a mesh with 32,292 elements and 146,077 degrees of freedom is used. A single element is selected to be distorted.

On each mesh, the Poisson equation with the exact solution u_2 is solved. The iterative solvers used are GMRES for AES-FEM and preconditioned conjugate gradient for FEM. The tolerance for both solvers is 10^{-12} . The preconditioner for AES-FEM is incomplete LU with a drop tolerance of 10^{-4} . Incomplete Cholesky factorization is the preconditioner for FEM, again with a drop tolerance of 10^{-4} .

The condition numbers of the stiffness matrices resulting from AES-FEM remain constant through the entire series of meshes. The condition numbers from FEM significantly increased as the quality of the mesh deteriorated. On the last two meshes, PCG stagnated for quadratic FEM. See Figure 8 for the condition numbers and the number of iterations required to solve the linear system. On the fourth mesh and every mesh thereafter, incomplete Cholesky encountered a nonpositive pivot and passed an error for cubic FEM. The solution errors remained practically constant for all methods considered.

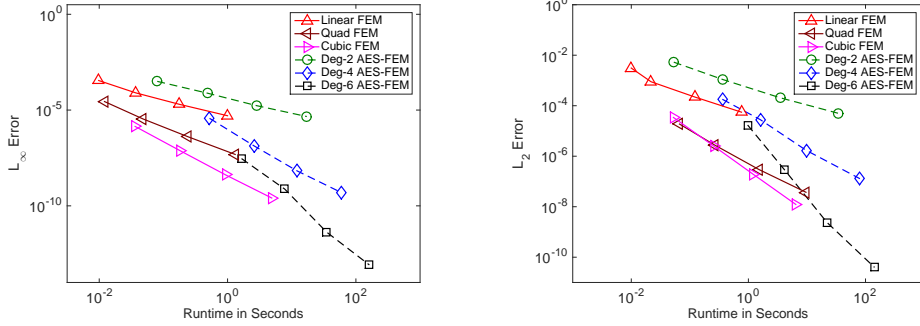


Figure 9: The errors verses runtime for 2D Poisson equation on the unit square for exact solution u_5 (left) and on the unit circle for exact solution u_4 (right).

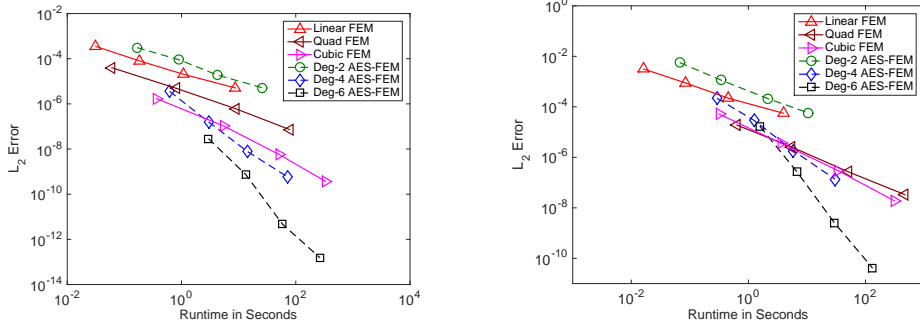


Figure 10: The errors verses runtime for 2D convection-diffusion equation on the unit square for exact solution u_5 (left) and on the unit circle for exact solution u_7 (right).

5.1.4 Efficiency

We compare the runtimes of degree two, four, and six AES-FEM and linear, quadratic, and cubic FEM for the Poisson and convection-diffusion equations on the unit square and the unit circle. Figures 9 and 10 show the errors versus runtimes for the 2-D Poisson equation and convection-diffusion equation on the unit cube, respectively. It is evident that degree-4 and degree-6 FEM outperform the quadratic and cubic FEM over finer meshes.

5.2 3-D Results

In this section, we describe the results of our experiments in 3D. For the Poisson and convection-diffusion equations, we consider a series of unstructured meshes. The linear meshes were created using TenGen [27] and range in size from 509 to 1,624,701 degrees of freedom. The high-order meshes were created with Gmsh

and range in size from 11,155 to 7,272,811 degrees of freedom. For any element in any of the meshes on the unit cube, the maximum dihedral angle is 166.05 degrees, the minimum dihedral angle is 6.09 degrees, and the maximum aspect ratio is 16.80, where the aspect ratio of an element is defined to be the ratio of the element's longest edge to its shortest height. For the meshes on the sphere, the maximum dihedral angle is 179.37 degrees, the minimum dihedral angle is 0.35 degrees and the maximum aspect ratio is 211.59.

5.2.1 Poisson Equation

We first consider the Poisson equation with Dirichlet boundary conditions on the unit cube and on the unit sphere. That is,

$$-\nabla^2 u = f \quad \text{in } \Omega, \quad (33)$$

$$u = g \quad \text{on } \partial\Omega. \quad (34)$$

For the unit cube, where $\Omega = [0, 1]^3$, we consider the following three analytic solutions:

$$u_1 = 64x^3(1-x^3)y^3(1-y^3)z^3(1-z^3), \quad (35)$$

$$u_2 = \cos(\pi x)\cos(\pi y)\cos(\pi z), \quad (36)$$

$$u_3 = \frac{1}{\sinh \pi \cosh \pi \cosh \pi} \sinh(\pi x) \cosh(\pi y) \cosh(\pi z). \quad (37)$$

For the unit sphere, where $\Omega = \{(x, y, z) | x^2 + y^2 + z^2 \leq 1\}$, we consider the analytic solution u_3 and also

$$u_4 = \cos\left(\frac{\pi}{2}(x^2 + y^2 + z^2)\right).$$

The Dirichlet boundary conditions are derived from the analytic solutions. On the unit cube, the boundary conditions for u_1 are homogeneous and are non-homogeneous for u_2 and u_3 . On the unit sphere, they are non-homogenous for u_3 and homogenous for u_4 .

The L_∞ and L_2 norm errors for u_1 on the unit cube are displayed in Figure 11. The L_2 norm errors for u_2 and u_3 on the unit cube and for u_3 and u_4 on the unit sphere are in Figures 12 and 13 respectively. Quadratic AES-FEM and linear FEM are similar in terms on convergence rate, with quadratic AES-FEM having slightly lower errors. Quartic and degree 6 AES-FEM are more accurate than the quadratic and cubic FEM on the unit cube. On the unit circle, linear FEM is the least accurate. Quadratic FEM and quadratic AES-FEM have similar errors, with quadratic FEM converging at a faster rate. Quartic and degree 6 AES-FEM were the most accurate. We do not have results for cubic FEM because incomplete Cholesky preconditioner encountered a nonpositive pivot when factoring the cubic FEM stiffness matrix. The solver did not converge when Gauss-Seidel was used as a preconditioner.

For solving the linear system resulting from AES-FEM, we use GMRES with Gauss-Seidel as a preconditioner. For FEM, we use preconditioned conjugate

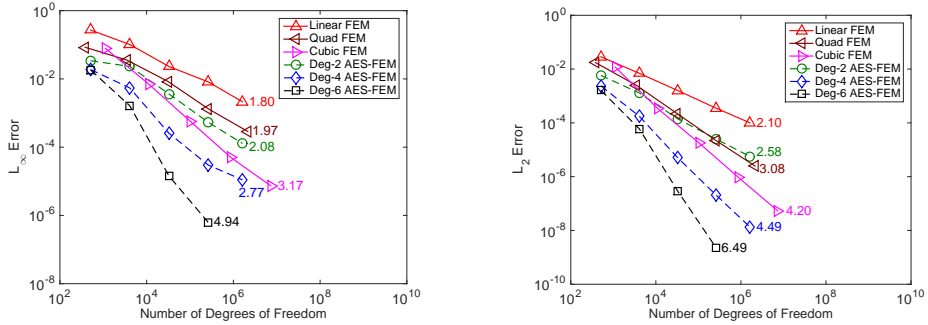


Figure 11: The errors for 3D Poisson equation on the unit cube for u_1 in the infinity norm (left) and L_2 norm (right).

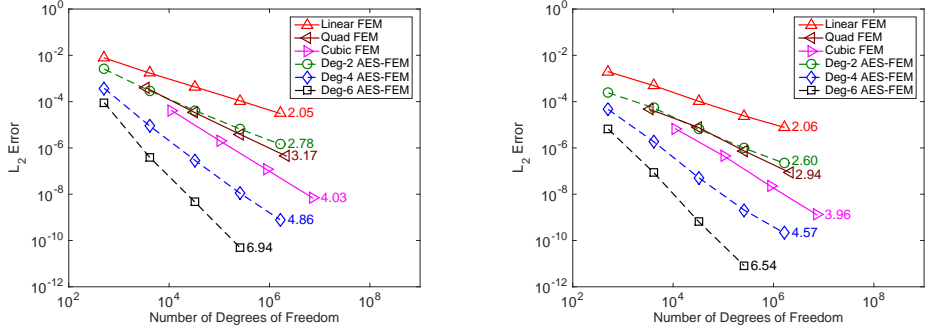


Figure 12: The L_2 norm errors for 3D Poisson equation on the unit cube for u_2 (left) and u_3 (right).

gradient. The preconditioner used is incomplete Cholesky with a drop tolerance of 10^{-3} on the unit cube and 10^{-6} on the unit sphere. The tolerance for the solvers is 10^{-12} .

5.2.2 Convection-Diffusion Equation

We consider the time-independent convection-diffusion equation with Dirichlet boundary conditions on the unit cube and the unit circle, that is,

$$-\nabla^2 u + \mathbf{c} \cdot \nabla u = f \quad \text{in } \Omega, \quad (38)$$

$$u = g \quad \text{on } \partial\Omega. \quad (39)$$

We take $\mathbf{c} = [1, 1, 1]^T$ and we consider the same analytic solutions as for the Poisson equation. Again, the Dirichlet boundary conditions are derived from the analytic solutions u_1, u_2, u_3 and u_4 .

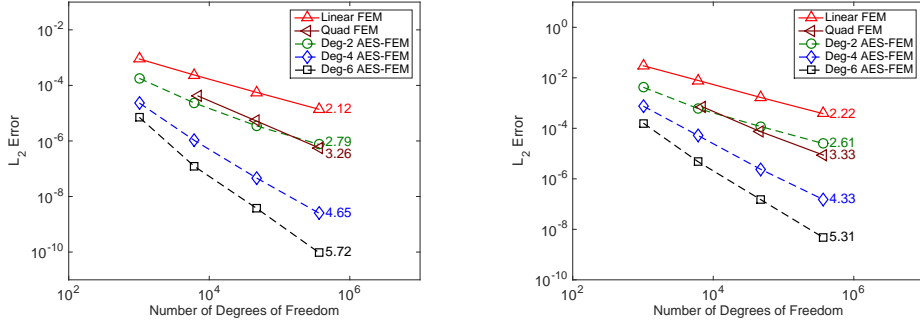


Figure 13: The L_2 norm errors for 3D Poisson equation on the unit sphere for u_3 (left) and u_4 (right).

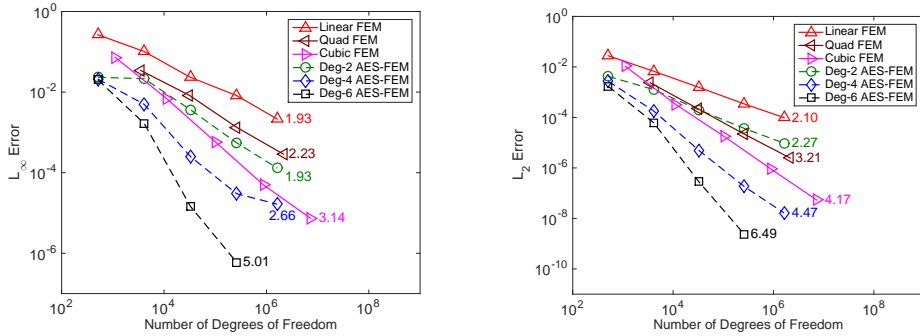


Figure 14: The errors for 3D convection-diffusion equation on the unit cube for u_1 in the infinity norm (left) and L_2 norm (right).

The L_∞ and L_2 norm errors for u_1 on the unit cube are displayed in Figure 14. The L_2 norm errors for u_2 and u_3 on the unit square and for u_3 and u_4 on the unit circle are in Figures 15 and 16 respectively. On the unit cube, linear FEM is the least accurate. Quadratic FEM and quadratic AES-FEM have similar errors, with quadratic FEM converging at a faster rate. On the unit sphere, cubic FEM performs the worse. Linear and quadratic FEM have higher errors than quadratic, quartic and degree 6 AES-FEM.

For solving the linear system resulting from AES-FEM, we use GMRES with a tolerance of 10^{-12} and Gauss-Seidel as the preconditioner. For u_1 on the unit cube, the solver stagnated for cubic FEM on the finer mesh. For u_4 on the unit sphere, the solver stagnates for quadratic FEM on the finer mesh.

5.2.3 Assessment of Element-Quality Dependence

We assess the dependence of AES-FEM and FEM on element quality by solving the Poisson equation with each method on a series of meshes with progressively

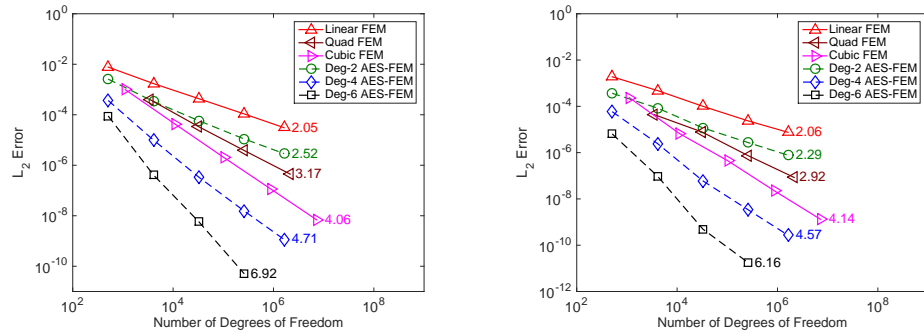


Figure 15: The L_2 norm errors for 3D convection-diffusion equation on the unit cube for u_2 (left) and u_3 (right).

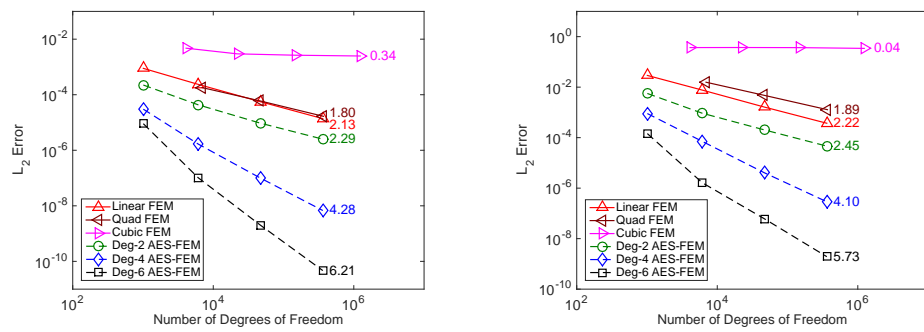


Figure 16: The L_2 norm errors for 3D convection-diffusion equation on the unit sphere for u_3 (left) and u_4 (right).

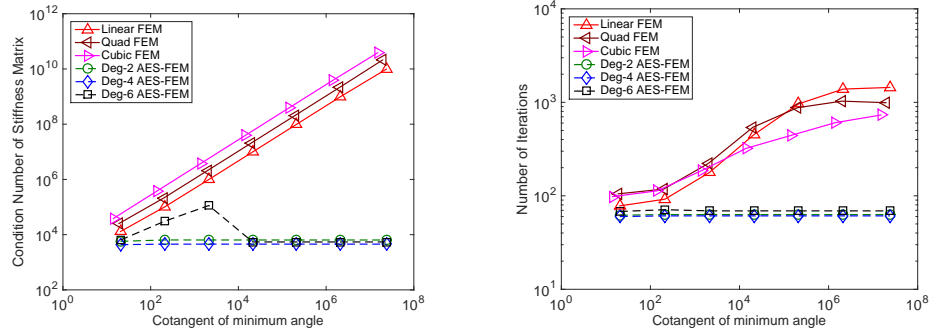


Figure 17: The lower bound of the condition numbers (left) of the stiffness matrices of FEM and AES-FEM method on a series of progressive worse meshes in 3D. The number of iterations (right) required for the iterative solver to converge when solving the corresponding systems.

worse element quality. We consider the condition numbers of the resulting stiffness matrices, the number of iterations needed to solve the resulting system, and the errors of the solutions. For all the methods, 0.005 percent of the total number of elements in the mesh are selected to be distorted. Within the selected elements, one vertex is moved incrementally towards its opposite edge. For linear FEM and AES-FEM with degree two, four, and six basis functions, we use a mesh with 1,604,418 elements and 190,978 degrees of freedom. Seventy-four elements are selected. For quadratic FEM, we use a mesh with 178,746 elements and 250,047 degrees of freedom. Nine elements are selected to be distorted. For cubic FEM, a mesh with 20,250 elements and 97,336 degrees of freedom is used. A single element is selected to be distorted.

On each mesh, the Poisson equation with the exact solution u_2 is solved. The iterative solvers used are GMRES for AES-FEM and preconditioned conjugate gradient for FEM. The tolerance for both solvers is 10^{-8} . The preconditioner used for both methods is Gauss-Seidel.

5.2.4 Efficiency

We compare the runtimes of degree two, four, and six AES-FEM and linear, quadratic, and cubic FEM. Figures 18 and 19 show the errors versus runtimes for the 3-D Poisson equation and convection-diffusion equation on the unit cube, respectively. It is evident that degree-4 and degree-6 FEM outperform the quadratic and cubic FEM over finer meshes.

6 Conclusions and Future Work

In this paper, we present a high-order extension of adaptive extended stencil finite element method (AES-FEM). AES-FEM uses generalized Lagrange poly-

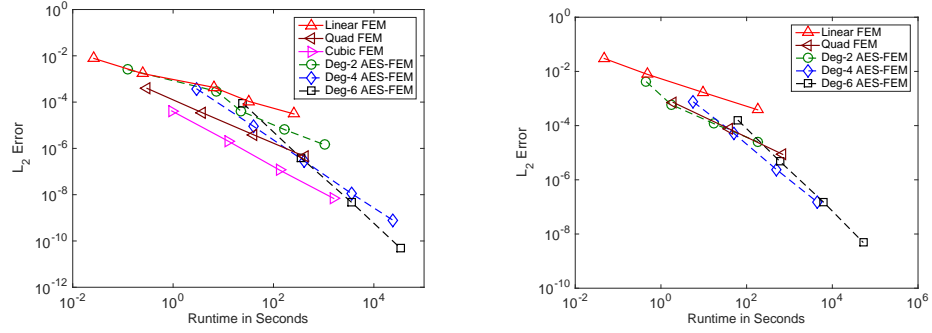


Figure 18: The errors verses runtime for 3D Poisson equation on the unit cube for exact solution u_5 (left) and on the unit sphere for exact solution u_4 (right).

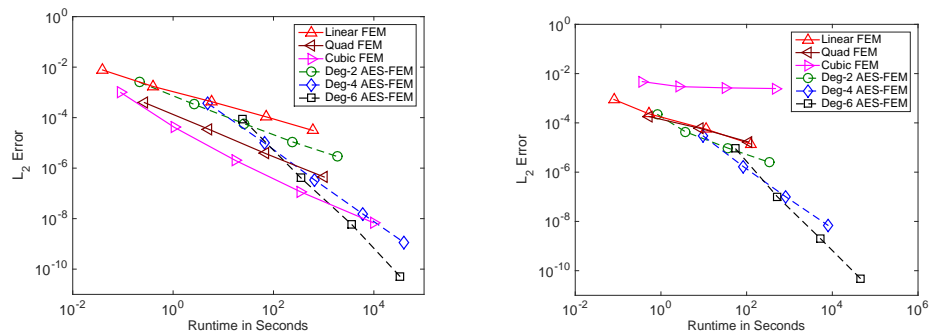


Figure 19: The errors verses runtime for 3D convection-diffusion equation on the unit cube for exact solution u_5 (left) and on the unit sphere for exact solution u_3 (right).

nomial basis functions constructed from weighted least-squares approximations and utilizes meshes with linear elements. The method is independent of element quality and preserves the theoretical framework of the classical FEM. Additionally, essential boundary conditions and integrating the stiffness matrix can be done in the same fashion as FEM. We compared the accuracy of AES-FEM with degree-2, 4, and 6 basis functions against FEM with linear, quadratic, and cubic basis functions for the Poisson equation and the time-independent convection-diffusion equation in 2D and 3D, including on domains with curved boundaries. We showed improved accuracy and stability of high-order AES-FEM over high-order FEM. We demonstrated that AES-FEM could achieve sixth order convergence, despite the use of linear elements. We demonstrated that the condition number of the stiffness matrix, and hence the number of iterations required to solve the system, resulting from AES-FEM is independent of the element quality. Additionally, we compared the efficiency of the method by considering the errors versus run time. AES-FEM is more efficient on finer meshes than FEM.

The present implementation of AES-FEM uses the standard hat functions as the weight functions, which may lead to large errors when applied to tangled meshes with inverted elements. We will report the resolution of tangled meshes in a future publication. Finally, while AES-FEM is efficient in terms of error versus runtime, it is much slower than the classical FEM on a given mesh due to the slower computation of the basis functions and the nonsymmetry of the stiffness matrix. The efficiency can be improved substantially by leveraging the parallelism and the efficient multigrid solvers, which we will report in the future.

Acknowledgements

This work was partially supported by DoD-ARO under contract #W911NF0910306. The third author is also supported by a subcontract to Stony Brook University from Argonne National Laboratory under Contract DE-AC02-06CH11357 for the SciDAC program funded by the Office of Science, Advanced Scientific Computing Research of the U.S. Department of Energy.

Results in this paper were obtained using the high-performance LIred computing system at the Institute for Advanced Computational Science at Stony Brook University, which was obtained through the Empire State Development grant NYS #28451.

References

- [1] D. N. ARNOLD, F. BREZZI, B. COCKBURN, AND L. D. MARINI, *Unified analysis of discontinuous Galerkin methods for elliptic problems*, SIAM J. Numer. Anal., 39 (2002), pp. 1749–1779.
- [2] I. BABUSKA, B. A. SZABO, AND I. N. KATZ, *The p -version of the finite element method*, SIAM J. Numer. Anal., 18 (1981), pp. 515–545.

- [3] F. BASSI AND S. REBAY, *A high-order accurate discontinuous finite element method for the numerical solution of the compressible Navier–Stokes equations*, J. Comput. Phys., 131 (1997), pp. 267–279.
- [4] F. BASSI AND S. REBAY, *High-order accurate discontinuous finite element solution of the 2D Euler equations*, J. Comput. Phys., 138 (1997), pp. 251–285.
- [5] C. CANUTO, M. Y. HUSSAINI, A. M. QUARTERONI, A. THOMAS JR, ET AL., *Spectral methods in fluid dynamics*, Springer Science & Business Media, Berlin Heidelberg, 2012.
- [6] F. CAZALS AND M. POUGET, *Estimating differential quantities using polynomial fitting of osculating jets*, Comput. Aid. Geom. Des., 22 (2005), pp. 121–146.
- [7] B. COCKBURN, J. GOPALAKRISHNAN, AND R. LAZAROV, *Unified hybridization of discontinuous Galerkin, mixed, and continuous Galerkin methods for second order elliptic problems*, SIAM J. Numer. Anal., 47 (2009), pp. 1319–1365.
- [8] B. COCKBURN, G. E. KARNIADAKIS, AND C.-W. SHU, *The Development of Discontinuous Galerkin Methods*, Springer, 2000.
- [9] R. CONLEY, T. J. DELANEY, AND X. JIAO, *Overcoming element quality dependence of finite elements with adaptive extended stencil FEM (AES-FEM)*, Int. J. Numer. Meth. Engng., (2016 (Accepted)).
- [10] L. DEMKOWICZ, W. RACHOWICZ, AND P. DEVLOO, *A fully automatic hp-adaptivity*, SIAM J. Sci. Comput., 17 (2002), pp. 117–142.
- [11] V. DYEDOV, N. RAY, D. EINSTEIN, X. JIAO, AND T. J. TAUTGES, *AHF: Array-based half-facet data structure for mixed-dimensional and non-manifold meshes*, in Proceedings of the 22nd International Meshing Roundtable, Springer, Orlando, Florida, 2014, pp. 445–464.
- [12] I. ERGATOUDIS, B. IRONS, AND O. ZIENKIEWICZ, *Curved, isoparametric, “quadrilateral” elements for finite element analysis*, Int. J. Solids Struct., 4 (1968), pp. 31–42.
- [13] B. A. FINLAYSON, *The Method of Weighted Residuals and Variational Principles*, Academic Press, New York, 1973.
- [14] A. GARGALLO-PEIRÓ, X. ROCA, J. PERAIRE, AND J. SARRATE, *Defining quality measures for validation and generation of high-order tetrahedral meshes*, in Proceedings of the 22nd International Meshing Roundtable, Springer, 2014, pp. 109–126.
- [15] C. GEUZAIN AND J.-F. REMACLE, *Gmsh: A 3-d finite element mesh generator with built-in pre-and post-processing facilities*, Int. J. Numer. Meth. Engng., 79 (2009), pp. 1309–1331.

- [16] G. H. GOLUB AND C. F. VAN LOAN, *Matrix Computations*, Johns Hopkins, Baltimore, 4th ed., 2013.
- [17] T. J. HUGHES, J. A. COTTRELL, AND Y. BAZILEVS, *Isogeometric analysis: CAD, finite elements, NURBS, exact geometry and mesh refinement*, Comput. Meth. Appl. Mech. Engrg., 194 (2005), pp. 4135–4195.
- [18] X. JIAO AND H. ZHA, *Consistent computation of first-and second-order differential quantities for surface meshes*, in ACM Symposium on Solid and Physical Modeling, ACM, 2008, pp. 159–170.
- [19] A. JOHNEN, J.-F. REMACLE, AND C. GEUZAIN, *Geometrical validity of curvilinear finite elements*, J. Comput. Phys., 233 (2013), pp. 359–372.
- [20] R. PASQUETTI AND F. RAPETTI, *Spectral element methods on triangles and quadrilaterals: comparisons and applications*, J. Comput. Phys., 198 (2004), pp. 349–362.
- [21] ———, *Spectral element methods on unstructured meshes: which interpolation points?*, Numer. Algorithms, 55 (2010), pp. 349–366.
- [22] A. T. PATERA, *A spectral element method for fluid dynamics: Laminar flow in a channel expansion*, J. Comput. Phys., 54 (1984), pp. 468–488.
- [23] J. PERAIRE AND P.-O. PERSSON, *The compact discontinuous Galerkin (CDG) method for elliptic problems*, SIAM J. Sci. Comput., 30 (2008), pp. 1806–1824.
- [24] P.-O. PERSSON AND J. PERAIRE, *Curved mesh generation and mesh refinement using Lagrangian solid mechanics*, in Proceedings of the 47th AIAA Aerospace Sciences Meeting and Exhibit, vol. 204, 2009.
- [25] R. SEVILLA, S. FERNÁNDEZ-MÉNDEZ, AND A. HUERTA, *NURBS-enhanced finite element method (NEFEM)*, Int. J. Numer. Meth. Engrg., 76 (2008), pp. 56–83.
- [26] J. R. SHEWCHUK, *Triangle: Engineering a 2D quality mesh generator and Delaunay triangulator*, in Applied Computational Geometry Towards Geometric Engineering, Springer, 1996, pp. 203–222.
- [27] H. SI, *TetGen, a Delaunay-based quality tetrahedral mesh generator*, ACM Trans. Math. Software, 41 (2015), pp. 11:1 – 11:36.
- [28] P. ŠOLÍN, J. ČERVENÝ, AND I. DOLEŽEL, *Arbitrary-level hanging nodes and automatic adaptivity in the hp-FEM*, Math. Comput. Simulat., 77 (2008), pp. 117–132.
- [29] P. ŠOLÍN, K. SEGETH, AND I. DOLEŽEL, *Higher-order finite element methods*, CRC Press, 2003.

- [30] B. SZABO AND A. MEHTA, *p -convergent finite element approximations in fracture mechanics*, Int. J. Numer. Meth. Engng., 12 (1978), pp. 551–560.
- [31] M. A. TAYLOR AND B. WINGATE, *A generalized diagonal mass matrix spectral element method for non-quadrilateral elements*, Appl. Numer. Math., 33 (2000), pp. 259–265.
- [32] T. TOULORGE, C. GEUZAIN, J.-F. REMACLE, AND J. LAMBRECHTS, *Robust untangling of curvilinear meshes*, J. Comput. Phys., 254 (2013), pp. 8–26.
- [33] P. VINCENT AND A. JAMESON, *Facilitating the adoption of unstructured high-order methods amongst a wider community of fluid dynamicists*, Math. Model. Nat. Phenom., 6 (2011), pp. 97–140.
- [34] D. WANG, B. CLARK, AND X. JIAO, *An analysis and comparison of parameterization-based computation of differential quantities for discrete surfaces*, Comput. Aid. Geom. Des., 26 (2009), pp. 510–527.
- [35] Z. WANG, *High-order methods for the Euler and Navier–Stokes equations on unstructured grids*, Prog. Aerosp. Sc., 43 (2007), pp. 1–41.
- [36] N. ZANDER, T. BOG, S. KOLLMANNSSBERGER, D. SCHILLINGER, AND E. RANK, *Multi-level hp -adaptivity: high-order mesh adaptivity without the difficulties of constraining hanging nodes*, Comput. Mech., 55 (2015), pp. 499–517.
- [37] O. ZIENKIEWICZ, R. TAYLOR, AND J. ZHU, *The Finite Element Method: Its Basis and Fundamentals*, Butterworth-Heinemann, Oxford, 2013.